

Mechanism of Vorticity Generation in Plasma Streamwise Vortex Generators

Michael Wicks,* Flint O. Thomas,[†] and Thomas C. Corke[‡]

University of Notre Dame, Notre Dame, Indiana 46556

and

Mehul Patel[§] and Alan B. Cain[§]

Innovative Technology Applications Company, LLC, Chesterfield, Missouri 63017

DOI: 10.2514/1.J053997

An experimental investigation into the mechanism of streamwise vorticity generation in an array of plasma streamwise vortex generators is presented. The array is flush mounted to a flat plate on which a nominally zero pressure gradient turbulent boundary layer develops upstream. The investigation is focused on characterization of the influence of freestream velocity, applied peak-to-peak voltage, length of the active electrode, and spanwise interelectrode spacing on streamwise vorticity generation. It is shown that the actuator creates wall-normal vorticity and reorients it into the streamwise direction. In addition, spanwise boundary-layer vorticity is reoriented into the streamwise direction. Scaling relations based on the vorticity transport equation are obtained and experimentally validated. These provide guidance for optimizing the actuators for particular flow control applications.

Nomenclature

A_v	=	vortex cross-sectional area in the y - z plane
E	=	electric field
E_{pp}	=	peak-to-peak excitation voltage
F_B	=	body force vector
L	=	active surface electrode length
M_∞	=	freestream Mach number
Re_x	=	Reynolds number
\bar{S}_{xj}	=	mean strain rate
s_{xj}	=	fluctuating strain rate
\bar{U}	=	streamwise mean velocity component
$\langle \bar{U} \rangle$	=	spanwise cycle-average mean velocity
U_∞	=	freestream velocity
u_j	=	j component velocity fluctuation
u_τ	=	wall friction velocity
\bar{V}	=	wall-normal mean velocity component
V_p	=	plasma-induced wall-normal velocity
\bar{W}	=	spanwise mean velocity component
\bar{W}_p	=	plasma-induced spanwise mean velocity
x, y, z	=	streamwise, wall-normal, and spanwise spatial coordinates, respectively
δ	=	99% boundary-layer thickness
δ^*	=	boundary-layer displacement thickness
λ	=	spanwise interelectrode spacing
$\Gamma(x)$	=	circulation
$\bar{\omega}_x$	=	streamwise component mean vorticity
ω'_x	=	streamwise vorticity fluctuation

I. Introduction

PASSIVE vortex generators (VGs) are widely used for separation control on both commercial and military aircraft. There are a wide variety of passive vane-type, surface-mounted VGs as reviewed by Lin [1] and Bushnell [2]. These often have vane heights on the order of the local boundary-layer thickness δ or smaller. Some designs create pairs of counter-rotating streamwise vortices, whereas others produce corotating vortices. Regardless of the details of their design, the production of near-wall streamwise vortices that persist over a significant downstream distance promotes cross-stream momentum transfer within the boundary layer. This serves to transport relatively high-momentum fluid from the outer region toward the wall and, consequently, the boundary layer is better able to withstand an imposed adverse pressure gradient without undergoing separation. Passive VGs have several advantages for flow control applications. They are simple, robust, proven devices that are easily retrofitted to the airframe. Their major detractor is a significant drag penalty incurred in portions of the flight envelope where they are not needed. For example, Martin et al. [3] showed that the combination of a transonic leading-edge glove (which lowered the local Mach number) and passive vortex generators was extremely effective at suppressing dynamic stall on a pitching airfoil. However, the effectiveness of the transonic glove and passive vortex generator combination diminished at higher Mach numbers above $M_\infty = 0.3$ – 0.4 as a result of shocks generated by the passive vortex generator. This suggests that passive VGs may give rise to a shock-induced drag penalty on the advancing rotor. In fact, there are many applications in which it is desirable to generate streamwise vorticity when boundary-layer separation is a possibility and have the VG effectively disappear when not needed. This is the basis of the plasma streamwise vortex generator (PSVG) actuators that are the focus of this paper.

The PSVG actuators are flush, surface-mounted active flow control actuators that are designed to use the body force vector field associated with dielectric barrier discharge (DBD) plasma actuation to create streamwise vorticity in a manner similar to passive VGs. Readers unfamiliar with application of DBD plasma actuators for aerodynamic flow control are referred to the recent comprehensive reviews on the subject by Corke et al. [4] and Moreau [5].

One of the first applications of PSVGs for aerodynamic flow control was reported by Huang et al. [6] in which plasma-induced streamwise vorticity was used for aeroacoustic control of a low-speed cavity resonance. More recently, Schatzman and Thomas [7] demonstrated the efficacy of PSVGs to eliminate separation of an adverse pressure gradient turbulent boundary developing on a convex ramp. PSVGs were also found to be quite effective in eliminating unsteady

Presented as Paper 2012-0824 at the 50th AIAA Aerospace Sciences Meeting, Nashville, TN, 9–12 January 2012; received 15 October 2014; revision received 31 March 2015; accepted for publication 13 May 2015; published online 30 July 2015. Copyright © 2015 by the American Institute of Aeronautics and Astronautics, Inc. All rights reserved. Copies of this paper may be made for personal or internal use, on condition that the copier pay the \$10.00 per-copy fee to the Copyright Clearance Center, Inc., 222 Rosewood Drive, Danvers, MA 01923; include the code 1533-385X/15 and \$10.00 in correspondence with the CCC.

*Graduate Research Assistant, Department of Aerospace & Mechanical Engineering, Institute for Flow Physics and Control. Member AIAA.

[†]Department of Aerospace & Mechanical Engineering, Institute for Flow Physics and Control. Associate Fellow AIAA.

[‡]Clark Equipment Professor, Department of Aerospace & Mechanical Engineering, Institute for Flow Physics and Control. Fellow AIAA.

[§]Associate Fellow AIAA.

vortex shedding from a circular cylinder in crossflow at high subcritical Reynolds numbers, as reported by Kozlov and Thomas [8], and in the aeroacoustic control of a tandem cylinder flow configuration by Kozlov and Thomas [9]. Okita et al. [10] reported delayed separation on a NACA 0024 airfoil due to the streamwise vortex produced by a single, yawed DBD actuator, which essentially functioned as a PSVG. Motivated by wind turbine applications, Jukes et al. [11] applied PSVG arrays to a NACA 4418 airfoil for separation control. They reported a 65% reduction in form drag and an increase in lift coefficient of $\Delta C_l = 0.4$ for experiments at a chord Reynolds number of 35,000.

A parametric investigation into DBD vortex generators was reported by Jukes and Choi [12]. The plasma vortex generator geometry used in that study was different from that used in this paper. It consisted of a single DBD plasma actuator whose surface electrode was placed at a yawed angle with respect to the oncoming flow direction. The plasma-induced spanwise wall jet interacted with the laminar boundary-layer flow to produce a streamwise vortex whose subsequent evolution was examined via particle image velocimetry (PIV) in local crossflow planes. DBD actuators producing both corotating and counter-rotating vortices were demonstrated. The effect of plasma-induced velocity, freestream velocity, surface electrode yaw angle, and length were systematically investigated. The benefits of electrode length and a yaw angle orthogonal to the oncoming flow were documented. The mechanism of streamwise vortex formation in a single electrode DBD plasma vortex generator was the topic of Jukes and Choi [13]. They found that a reorientation of laminar boundary-layer spanwise vorticity into the outer shear layer of the plasma-induced spanwise wall jet, combined with the considerable streamwise vorticity already present in the jet shear layer, was responsible for streamwise vortex formation.

Based upon the literature cited earlier, the efficacy of PSVGs for flow control has been demonstrated. In this paper, an experimental investigation into basic mechanisms governing the behavior of PSVG actuator arrays is presented. The focus of the work is to 1) gain a better understanding of the mechanism of vorticity generation and 2) to derive and experimentally verify scaling relations for these devices. The understanding gleaned from this investigation is considered a prerequisite to optimizing PSVG arrays for specific flow control applications.

The PSVG arrays are flush mounted to a flat plate on which a nominally zero pressure gradient (ZPG) turbulent boundary layer develops. Unlike the study by Jukes and Choi [12,13], which used a thin, 250 μm Mylar dielectric barrier, this study exploits the work of Thomas et al. [14], which demonstrated a better than order-of-magnitude increase in the plasma-induced body force produced by actuators using comparatively thick dielectric barriers. Consequently, the PSVGs in this study use a quartz dielectric of 3.18 mm (1/8 in.) thickness (≈ 13 times thicker than in [12,13]). This allows the application of much higher ac voltages than is possible with plasma actuators using thin-film dielectric barriers (in this case, up to 50 kV peak-to-peak). In fact, the lowest applied voltage in this study exceeded the maximum voltage of 12 kV peak-to-peak used in [12]. This is significant because it has been shown [4,14] that the body

force scales with the applied voltage to the 7/2 power. The PSVG array geometric design in this study is also very different than the single yawed DBD actuators used in [12,13], as detailed in the following section. Furthermore, the approach boundary layer is fully turbulent and the freestream flow velocity in the present study extends to 35 m/s, whereas most of the experimental results presented in [12] are for laminar boundary layers with very low freestream velocities (less than 2 m/s). Perhaps more significantly, the ratio of plasma-induced jet velocity \bar{W}_p to freestream velocity U_∞ was as high as 1.2 in [12]. In the current study, the values are $0.03 \leq \bar{W}_p/U_\infty \leq 0.07$ (two orders of magnitude smaller).

II. Experimental Apparatus and Procedures

A. Wind-Tunnel Facility

The PSVG experimental investigation was performed in one of the low-turbulence, subsonic in-draft wind tunnels located at the Hessert Laboratory for Aerospace Research at the University of Notre Dame. The wind tunnel has an inlet contraction ratio of 20:1. A series of 12 turbulence management screens at the front of the inlet give rise to tunnel freestream turbulence levels of less than 0.1% (0.06% for frequencies above 10 Hz). The maximum tunnel speed is approximately $U_\infty = 40$ m/s. Experiments are performed in a test section of 0.61 m (2 ft.) square cross-section and 1.82 m (6 ft) in length. One test section and the ceiling have optical access for nonintrusive laser flowfield diagnostics [in this study, laser Doppler anemometry (LDA) or PIV].

B. Experimental Test Fixture

A schematic of the test fixture is shown in Figs. 1a and 1b, whereas Fig. 1c presents a rendered CAD model. The PSVG test fixture consists of a flat acrylic boundary-layer development plate that is 1.2 m (48 in.) in length, 0.6 m (24 in.) in width, and 1 cm (0.4 in.) thick with a rounded leading-edge containing distributed sand grain roughness to promote rapid boundary-layer transition (labeled 1 in Fig. 1). The last 0.2 m length of the plate consists of a 2.2 deg linear, symmetric taper down to a trailing-edge thickness of 1.6 mm (labeled 2 in Fig. 1). The plate was sidewall mounted and spanned the wind-tunnel test section. As shown in Fig. 1, a PSVG actuator test fixture (labeled 3 in Fig. 1) was flush mounted into a cavity machined into the plate surface at a location 0.79 m (31 in.) downstream of the leading-edge. This streamwise distance from the leading-edge allows for nominally ZPG turbulent boundary-layer growth before application of PSVG flow control. The cavity provides ample room for accommodating both the required high-voltage leads and the dielectric barrier material that forms the PSVG. Figure 2c shows a close-up view of one of the PSVG arrays ready for installation into the plate cavity. A full description of the PSVG geometry and details regarding construction are presented in the following section.

C. Plasma Streamwise Vortex Generator Array

The basic geometry of the PSVG arrays examined in this study is shown schematically in Fig. 2. As indicated in the figure, this configuration uses a common covered electrode, which is separated

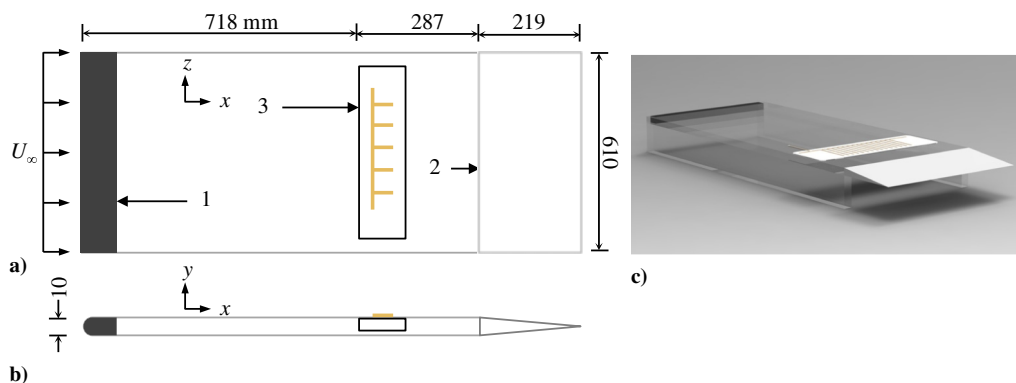


Fig. 1 Experimental test fixture: a) top view schematic, b) side view schematic, and c) rendered CAD model.

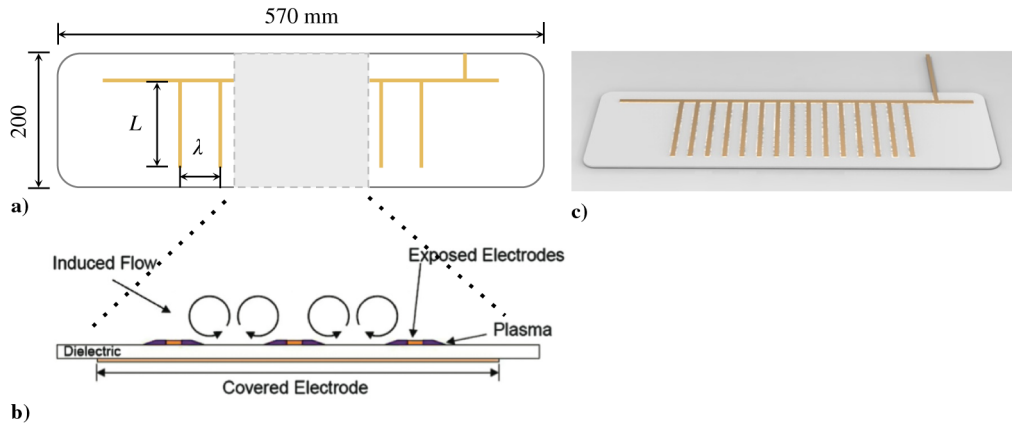


Fig. 2 Schematic of PSVG array geometry: a) top view, b) streamwise view, and c) close up of a PSVG array insert.

from the exposed electrodes by a sheet of dielectric barrier material. The multiple exposed (surface) electrodes with streamwise length L and spanwise interelectrode spacing λ are aligned parallel to the oncoming flow. Because of the use of a common covered electrode, plasma forms on both sides of each surface electrode. It will be shown that the resulting body force gives rise to a series of opposing wall jets in the spanwise direction that collide and interact with the external flow, thereby generating pairs of counter-rotating streamwise vortices with size $O(\lambda/2)$ as indicated in Fig. 2b. These become the basis for enhanced cross-stream mixing of momentum within the boundary layer for separation control. The electrode array shown in Fig. 2 for the generation of streamwise vorticity is obviously quite different from the single streamwise-oriented DBD actuator investigated by Jukes and Choi [13].

As noted earlier, the dielectric material used in this study was quartz of 3.2 mm thickness (1/8 in.). The dielectric material extended 0.57 m (22.5 in.) in the spanwise direction and 20.3 cm (8 in.) in the streamwise direction. Each plasma actuator electrode consisted of copper foil tape of 0.05 mm thickness. Each of the streamwise-oriented exposed electrodes extended from a common spanwise surface electrode upstream of the covered electrode, as shown in Fig. 2a (no plasma forms on this spanwise electrode). In each case, the span was fixed at 46.4 cm (18.25 in.). Each exposed electrode is 3.2 mm (1/8 in.) in width and has a length of 15.24 cm (6 in.). The streamwise length of the covered electrode was varied in this investigation. This controlled the streamwise extent of the plasma forming region on each surface electrode. Streamwise lengths of 2.54, 5.08, 10.2, and 15.24 cm (1, 2, 4, and 6 in.) were examined.

Both the covered electrode and exposed electrode were connected to high-voltage wires that led out of the test fixture and connected to the transformers of the plasma generation circuit. The circuit used to operate the PSVG array is identical to that presented in Kozlov and Thomas ([8] Fig. 6). Unless otherwise noted, the actuators were operated with an ac carrier consisting of a sinusoidal waveform of 2 kHz frequency and a peak-to-peak voltage that was varied from 15 to 50 kV.

D. Flowfield Diagnostics

This study used standard, nonintrusive flowfield diagnostics in the form of LDA and PIV to characterize the vorticity generation by the PSVG arrays. These techniques are briefly described in this section.

LDA surveys of mean velocity in y - z crossflow planes were obtained both over and downstream of the PSVG arrays using a Dantec Dynamics Fiber Flow LDA system with a Spectra Physics Stabilite 2017 Argon-Ion Laser. The LDA system allows for cross-flow plane measurements of mean velocity at high freestream flow speeds, which would otherwise not be feasible with conventional planar or stereo PIV due to the dominant out-of-plane (streamwise) x -velocity component. The fiber optic LDA system was operated in full 180 deg backscatter mode. The Doppler bursts were measured using a BSA F60 flow processor and BSA Flow Software Version 4.10. The boundary-layer flow was seeded with Di-Ethyl-Hexyl-Sebacat (DEHS) particles of nominally 1 μ m diameter that were introduced

upstream of the wind-tunnel inlet contraction with a TSI Six-Jet Atomizer 9306.

At each streamwise measurement location, the fiber optic probe (using a 400 mm focal length lens) was traversed in a rectangular 30×25 mm grid in the local y - z crossflow plane using a three-axis Aerotech traverse system and Unidex 11 controller. The LDA probe measurement volume has a maximum wall-normal dimension of 0.38 mm and just over 1.3 mm in the spanwise direction. This effectively set the spatial resolution for the mean flow measurement.

The \bar{U} , \bar{V} , and \bar{W} mean velocity components were measured in a given cross-stream plane via two measurements at each y - z location. These were performed with the LDA transceiver head oriented at two separate oblique angles α_1 and α_2 (with respect to the boundary-layer development plate surface). A coordinate transformation related the measured mean velocities \bar{U}_1 , \bar{U}_2 , and \bar{U}_3 to measurements of \bar{U} , \bar{V} , and \bar{W} . In particular,

$$\begin{bmatrix} \bar{U}_1 \\ \bar{U}_2 \\ \bar{U}_3 \end{bmatrix} = \begin{bmatrix} 1 & 0 & 0 \\ 0 & \cos(\alpha_1) & \sin(\alpha_1) \\ 0 & \cos(\alpha_2) & \sin(\alpha_2) \end{bmatrix} \begin{bmatrix} \bar{U} \\ \bar{V} \\ \bar{W} \end{bmatrix} \quad (1)$$

The last two equations of Eq. (1) allow $\bar{V}(x; y, z)$ and $\bar{W}(x; y, z)$ to be determined from measured $\bar{U}_2(x; y, z)$ and $\bar{U}_3(x; y, z)$. The estimated relative uncertainty in the mean flow measurements at 20:1 odds was estimated to be $\pm 3.4\%$.

For mean flow measurements without external flow, a LaVision time-resolved PIV system was used to nonintrusively acquire two-component velocity data in selected y - z planes. The system consisted of a Litron LDY300 series neodymium-doped yttrium lithium fluoride pulse laser, a Photron SA 1.1 high-speed camera, and dedicated computer running DaVis 8.0 vector processing software. The laser light sheet was directed through the side window of the wind tunnel. Sheet optics consisting of a combination of a spherical and a cylindrical lens were used to create a 1-mm-thick light sheet at the measurement plane. The high-speed camera, equipped with a Nikon 105 mm lens and 2x teleconverter operating at $f/2.8$, was positioned on top of the test section, angled at approximately 30 deg to the actuator surface. This angular distortion was corrected with an appropriately aligned calibration plate, and calibrations were performed at each discrete x position. The interrogation region corresponded to physical domains of approximately 48 – 57×59 – 65 mm, depending on the calibration used. A TSI atomizer produced nominally 1- μ m-diam DEHS seed particles injected upstream of the wind-tunnel inlet via a mixing box, allowing for uniform particle dispersion in the measurement plane. The measurement uncertainty for the mean velocity and vorticity as measured with the PIV is estimated to be within 2 and 8%, respectively.

It should be noted that, for the electric fields encountered in these experiments, dimensional analysis confirms that the aerodynamic forces on the DEHS seed particles were several orders of magnitude greater than the electrostatic forces. Consistent with this, none of the LDA or PIV results suggested that seed particles follow electric field lines.

Table 1 Upstream boundary-layer parameters

U_∞ , m/s	$Re_x \times 10^6$	$\delta_{99\%}$, mm	δ^* , mm	θ , mm	H	C_f
15	0.75	34.8	4.93	3.57	1.38	0.0036
20	1.01	32.0	4.90	3.55	1.38	0.0034
25	1.26	31.4	4.87	3.52	1.38	0.0033
30	1.47	30.3	4.83	3.54	1.36	0.0033

E. Approach Turbulent Boundary-Layer Flow

The approach ZPG turbulent boundary-layer mean velocity profiles all showed excellent agreement with the Klebanoff [15] profile (obtained at much higher Re_x) as shown in Fig. 3 for a range of freestream velocities used in the experiment. Approach boundary-layer parameters are summarized in Table 1. It should be noted that shape factor and skin friction coefficient values were consistent with those for ZPG turbulent boundary layers at the given Re_x .

III. Experimental Results

In this section, key results from the experimental investigation into the behavior of several PSVG arrays are presented. Before presenting results for the PSVG operated with an approach turbulent boundary-layer flow, consideration is first given to the case of no external flow.

A. Quiescent Case Vorticity Generation

Before examining the interaction of the PSVG array with the oncoming boundary-layer flow, it is useful to consider how the actuators produce vorticity in the absence of an approach flow. To do this, PIV measurements of the actuator-induced flow were performed

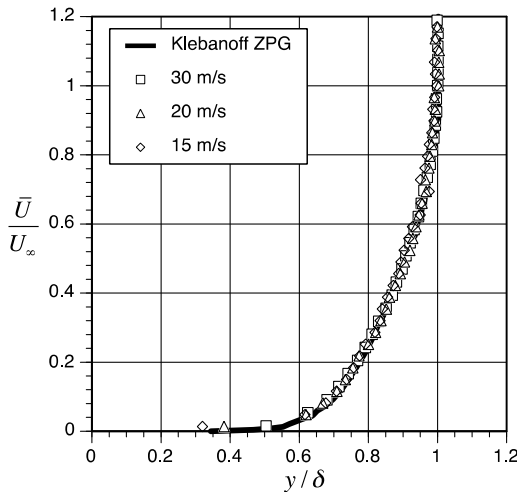


Fig. 3 Comparison of measured turbulent boundary-layer mean velocity profiles upstream of the PSVG array with that by Klebanoff [15].

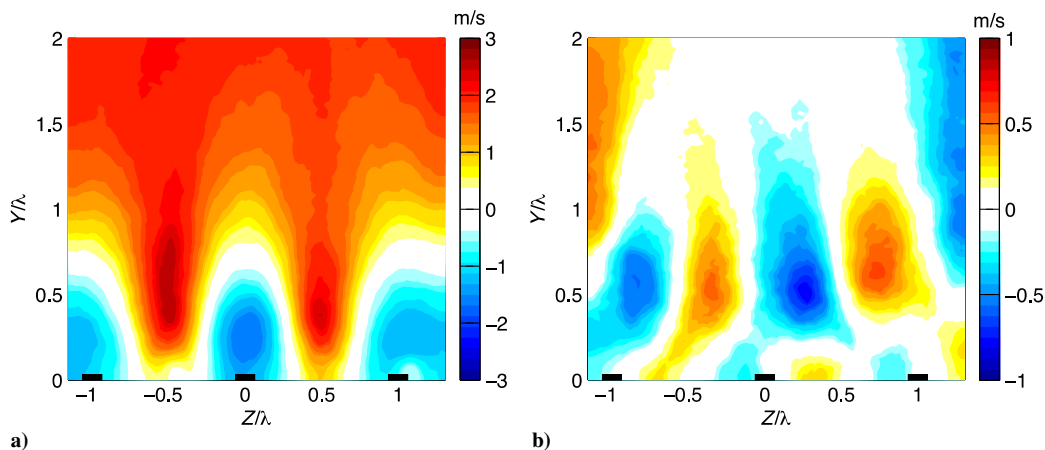


Fig. 4 Measured a) $\bar{V}(y,z)$ and b) $\bar{W}(y,z)$ induced by the PSVG array: $V_{pp} = 50$ kV, $\lambda = 25.4$ mm, $L = 101.6$ mm, $x/L = 0.5$.

in a y - z plane located at $x = L/2$ to avoid end effects. In this section, representative results are presented that serve to illustrate the generation of x -oriented vortices by the PSVG array.

The plasma-induced wall-normal $\bar{V}(x,y,z)$ and spanwise $\bar{W}(x,y,z)$ mean velocity components were measured in the $(x = L/2, y, z)$ crossflow plane and these were used to compute the local x -component mean vorticity $\bar{\omega}_x \equiv (\partial \bar{W}/\partial y - \partial \bar{V}/\partial z)$, induced by the actuators in the absence of any external flow.

Figures 4a and 4b present representative measurements of $\bar{V}(L/2, y, z)$ and $\bar{W}(L/2, y, z)$, respectively, for the case of an applied peak-to-peak voltage $E_{pp} = 35$ kV, an interelectrode spacing $\lambda = 25.4$ mm (1 in.), and covered electrode length $L = 101.6$ mm (4 in.). For reference, the surface electrode locations are indicated as dark rectangles on the abscissa. Figure 4a shows measured $\bar{V}(y, z)$ and indicates that the imposed actuator body force $F_B = \rho_c E$ draws ambient fluid downward toward each surface electrode. This, combined with the impermeability of the wall, gives rise to a series of opposing spanwise wall jets as shown in the $\bar{W}(y, z)$ measurements presented in Fig. 4b. The wall jets give rise to large values of $\partial \bar{W}/\partial y$ near the wall.

The maximum spanwise wall jet velocity induced by the PSVG array is approximately $\bar{W}_{pmax} \approx 1$ m/s. Experimental results presented in [14] for a comparable applied voltage and dielectric thickness show that this value of \bar{W}_{pmax} is approximately one-quarter to one-third of that which would be obtained for a conventional DBD plasma actuator in which plasma is allowed to form on only one side of the surface electrode. The reduced plasma-induced wall jet velocity for the PSVG is due to the (necessary) plasma formation on both sides of the surface electrode.

The opposing wall jets collide near the midpoint location between adjacent surface electrodes and this gives rise to a local upwelling of fluid, as shown in Fig. 4a. The maximum upwelling velocity is $\bar{V}_{pmax} \approx 2.5$ m/s. The requirement of mass conservation leads to divergent spanwise mean velocity \bar{W} near the top of the upwelling. The wall-directed motion of fluid over the electrodes, combined with the localized upwelling between, also gives rise to large values of $\partial \bar{V}/\partial z$.

Figure 5 presents the isovelocity contours of the mean velocity induced by the PSVG array and clearly shows the spanwise periodic nature of the actuator-induced mean flow pattern. In this manner, x -component vorticity $\bar{\omega}_x = (\partial \bar{W}/\partial y - \partial \bar{V}/\partial z)$ is created by the PSVG actuator as shown in the isovorticity contour map of Fig. 6. This figure clearly shows that a periodic array of counter-rotating x -oriented vortices is set up by the actuator-induced body force. Peak values of time-mean mean vorticity are observed to be approximately $\bar{\omega}_x \approx 250$ s $^{-1}$.

It is apparent from the measurements presented that the body force due to the actuator array acts in combination with the no-slip condition at the wall to produce x -directed vorticity in the quiescent case. However, it will be shown that the magnitude of peak x -directed (i.e., streamwise) vorticity is considerably larger when there is an

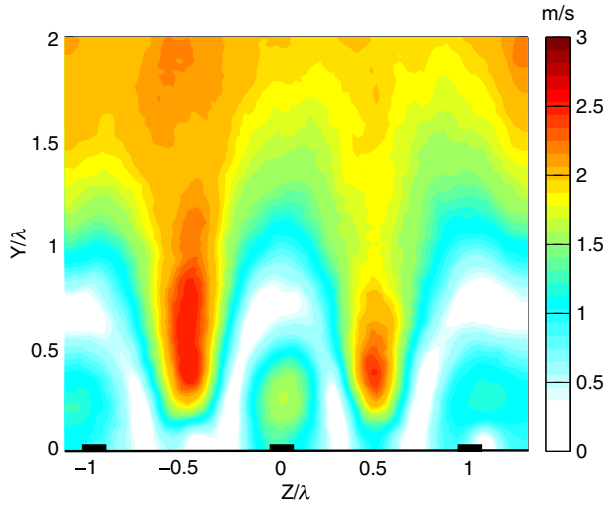


Fig. 5 Contours of PSVG actuator-induced velocity for the quiescent case: $V_{pp} = 50$ kV, $\lambda = 25.4$ mm, $L = 101.6$ mm, $x/L = 0.5$.

approach turbulent boundary-layer flow. This suggests that a primary mechanism for PSVG vorticity production involves the interaction of the plasma-generated flow with the oncoming boundary layer. The nature of this interaction mechanism will be the focus of the next section.

B. Mechanism of PSVG Streamwise Vorticity Generation: Scaling Relations

In this section, consideration is given to the mechanism of streamwise vorticity generation by the PSVG array when there is an approach boundary-layer flow. Scaling arguments will be used to demonstrate that a key element in this process is the interaction of the approach boundary-layer flow with the plasma-induced flow set up by the actuator body force vector.

Figure 7 shows contours of the time mean streamwise vorticity $\bar{\omega}_x$, created at the downstream end of a PSVG array for the case in which there is an approach turbulent boundary-layer flow. In particular, contours of $\bar{\omega}_x$ are presented in a y - z plane located at the downstream edge of the PSVG actuator for several values of freestream velocity, $10 \text{ m/s} \leq U_\infty \leq 30 \text{ m/s}$ with $L = 101.6$ mm, $\lambda = 2.54$ cm, $E_{pp} = 40$ kV, and $x/L = 1$. These data were acquired via laser Doppler anemometry using the method described in Sec. II.D. Figure 7 shows a qualitative resemblance to the mean vorticity field setup in the quiescent case described previously (see Fig. 6), but the reader will note that the streamwise vorticity magnitude produced with an approach boundary-layer flow is much larger. This indicates the important role played by the interaction with the approach boundary-

layer flow. Note that the wall-normal coordinate is scaled by the local boundary-layer thickness δ , and Fig. 7 indicates that the vortices are confined within the turbulent boundary layer. It is easy to show that, for a pair of potential vortices in proximity to a horizontal wall, there is a self-induced motion of the vortex pair in the wall-normal direction, which at fixed circulation Γ is directly proportional to time. In this experiment, L was fixed and U_∞ was varied and so, not surprisingly, Fig. 7 shows that the greatest wall-normal extent of streamwise vorticity is associated with the largest convective time-scale L/U_∞ . For example, at $U_\infty = 10$ m/s, streamwise vorticity extends to $y/\delta \approx 0.4$. Conversely, at the highest freestream speed and smallest convective time-scale, the streamwise vorticity is largely confined to the near-wall region $y/\delta \leq 0.15$.

To examine the generation of mean streamwise vorticity $\bar{\omega}_x$ by the PSVG array, consideration is given to the x -component mean vorticity transport equation, which is given by

$$\frac{D\bar{\omega}_x}{Dt} = \bar{\omega}_j \bar{S}_{xj} + \overline{\omega'_j s'_{xj}} - u_j \overline{\frac{\partial \omega'_x}{\partial x_j}} + \nu \frac{\partial^2 \bar{\omega}_x}{\partial x_j \partial x_j} \quad (2)$$

The actuator array is operated in a quasi-steady manner and focus will be given to its influence on the time mean flow as illustrated in Fig. 7. In this context, the primary streamwise vorticity generation occurs through the mean vorticity-strain rate interaction terms $\bar{\omega}_j \bar{S}_{xj}$. In contrast, the vorticity fluctuation-fluctuating strain rate correlation $\overline{\omega'_j s'_{xj}}$ and fluctuating velocity-vorticity gradient correlation $u_j \overline{\partial \omega'_x / \partial x_j}$ on the right-hand side of Eq. (2) are largely responsible for turbulent vorticity redistribution mechanisms that occur within the boundary layer downstream of the actuator. Further, viscous diffusion is neglected because, for high Reynolds number flow, it operates on timescales that are much longer than the mean vorticity-mean strain rate interaction terms. Hence, focus is given to the terms

$$\bar{\omega}_j \bar{S}_{xj} = \bar{\omega}_x \bar{S}_{xx} + \bar{\omega}_y \bar{S}_{xy} + \bar{\omega}_z \bar{S}_{xz} \quad (3)$$

In the nominally zero-pressure gradient turbulent boundary layer under consideration here, streamwise dilatation is negligible, $\bar{S}_{xx} = 0$. Hence, focus is given to the two remaining terms, $\bar{\omega}_y \bar{S}_{xy} = \bar{\omega}_y \partial \bar{U} / \partial y$ and $\bar{\omega}_z \bar{S}_{xz} = \bar{\omega}_z \partial \bar{U} / \partial z$. The former term serves to take wall-normal mean vorticity and reorient it into the streamwise direction. The latter term does the same for initially spanwise-oriented mean vorticity.

The wall-normal time mean vorticity $\bar{\omega}_y \equiv \partial \bar{U} / \partial z - \partial \bar{W} / \partial x$ in the zero pressure gradient turbulent boundary layer upstream of the actuator is expected to be negligible, and this was confirmed experimentally. However, as shown in the sample $\bar{U}(y, z)$ isocontour measurements obtained at the downstream edge of the PSVG array presented in Fig. 8, the plasma-induced body force draws ambient fluid toward the surface electrodes and also gives rise to wall-normal flow away from the wall at locations midway between adjacent electrodes. The combined effect serves to create wall-normal vorticity through the production of nonzero $\partial \bar{U} / \partial z$.

To further characterize $\partial \bar{U} / \partial z$, the LDV probe volume was traversed in the spanwise z direction at a fixed distance of 7.62 cm (3 in.) downstream of the PSVG array, with the wall-normal height fixed at δ^* , the local boundary-layer displacement thickness. Figure 9 presents the spanwise variation of mean velocity $\bar{U}(\delta^*, z)$ downstream of the PSVG array for external velocities ranging from $10 \leq U_\infty \leq 30$ m/s (corresponding to the Reynolds number range of $0.54 \text{ million} \leq Re_x \leq 1.61 \text{ million}$). Traverses at several other wall-normal locations were also performed, and the results in Fig. 9 may be considered representative. The spanwise variation is observed to be quasi periodic. To account for the variation in external velocity between trials, the measurements are presented by subtracting the spanwise cycle-average mean velocity $\langle \bar{U} \rangle$ and normalizing by the external velocity U_∞ . The location $z = 0$ is centered midway between adjacent surface electrodes (electrode locations are shown on the abscissa). Figure 9 shows that this normalization provides a remarkable collapse for all the cases. Negative peaks are centered

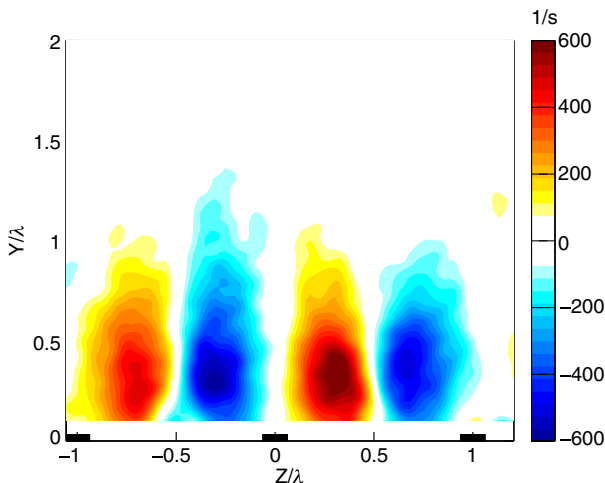


Fig. 6 Contours of x -directed vorticity produced by PSVG array in quiescent case: $V_{pp} = 50$ kV, $\lambda = 25.4$ mm, $L = 101.6$ mm, $x/L = 0.5$.

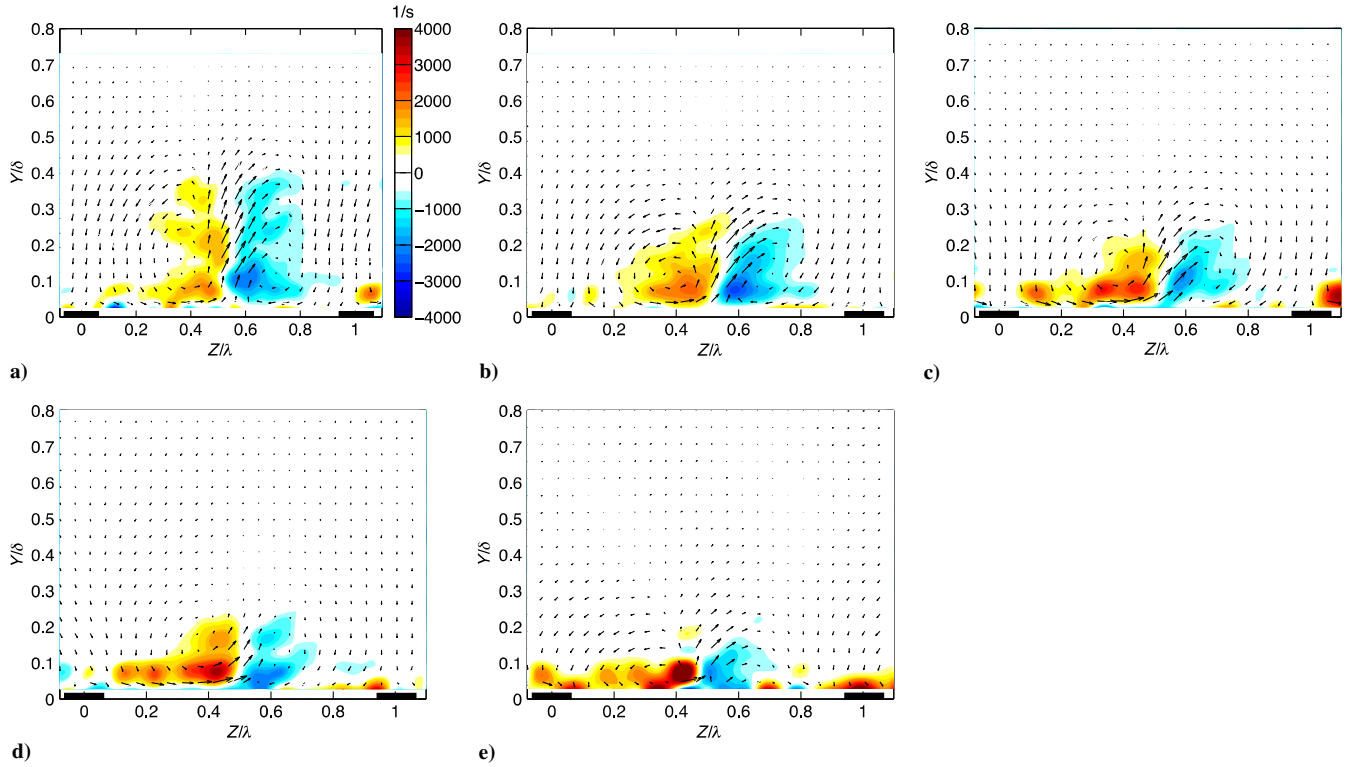


Fig. 7 Mean streamwise vorticity contours and velocity vectors at $U_\infty =$ a) 10, b) 15, c) 20, d) 25, and e) 30 m/s. PSVG electrodes drawn schematically in black.

between the surface electrodes and are associated with the local upwelling of comparatively low-velocity fluid from the near-wall region due to colliding spanwise plasma-induced wall jets (as also seen in Fig. 8). In contrast, broader positive excursions are centered over the surface electrodes and are associated with transport of comparatively high-velocity fluid downward toward the surface electrodes by the plasma-induced body force. Because of the similarity scaling demonstrated in Fig. 9, the ordinate may be denoted as $F(z)$, and it follows that $\partial \bar{U} / \partial z = U_\infty dF / dz$. That is, the spanwise mean velocity gradient set up by the PSVG array $\partial \bar{U} / \partial z$ is directly proportional to U_∞ . This aspect will be used in scaling arguments developed later in this section.

As a consequence of the spanwise mean velocity gradient set up by the PSVG array, we have $\bar{\omega}_y \bar{S}_{xy} \approx (\partial \bar{U} / \partial z)(\partial \bar{U} / \partial y)$. Consider next the term $\bar{\omega}_z \bar{S}_{xz} \approx \bar{\omega}_z \partial \bar{U} / \partial z$. To good approximation, the mean

spanwise vorticity in the turbulent boundary layer is $\bar{\omega}_z \approx \partial \bar{U} / \partial y$. Hence, we have $\bar{\omega}_z \bar{S}_{xz} \approx (\partial \bar{U} / \partial y)(\partial \bar{U} / \partial z)$, and so it follows that both of the relevant vorticity-strain rate interaction terms involve the product of mean velocity gradients in the wall-normal and spanwise directions. For the vorticity redistribution mechanism, the required $\partial \bar{U} / \partial y$ is provided primarily by the approach boundary-layer flow, whereas the plasma-induced body force associated with the PSVG array creates the required spanwise gradients in mean velocity $\partial \bar{U} / \partial z$, as illustrated in Figs. 8 and 9.

The approach turbulent boundary-layer mean spanwise vorticity

$$\bar{\omega}_z = \frac{\partial \bar{U}}{\partial y} \approx O\left(\frac{U_\infty}{\delta^*}\right) \quad (4)$$

where δ^* is the displacement thickness (i.e., the wall-normal centroid of spanwise vorticity for the turbulent boundary layer). This is an intermediate strain rate scaling that is much less than the limiting

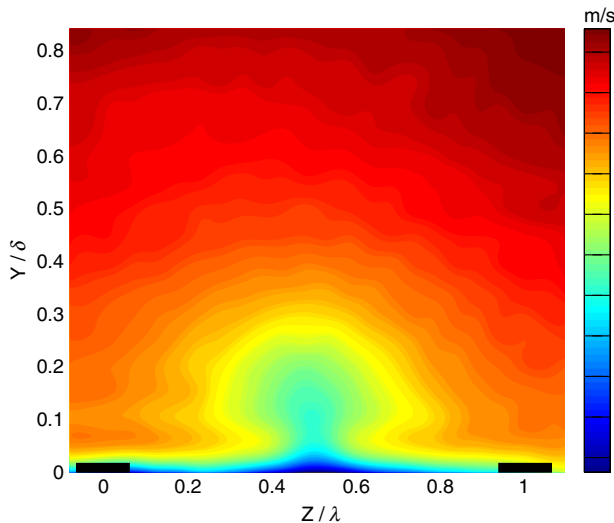


Fig. 8 Streamwise mean velocity contours measured at downstream edge of PSVG array for case of $U_\infty = 30$ m/s, $E_{pp} = 40$ kV, $\lambda = 25.4$ mm, $x/L = 1$, $L = 101.6$ mm.

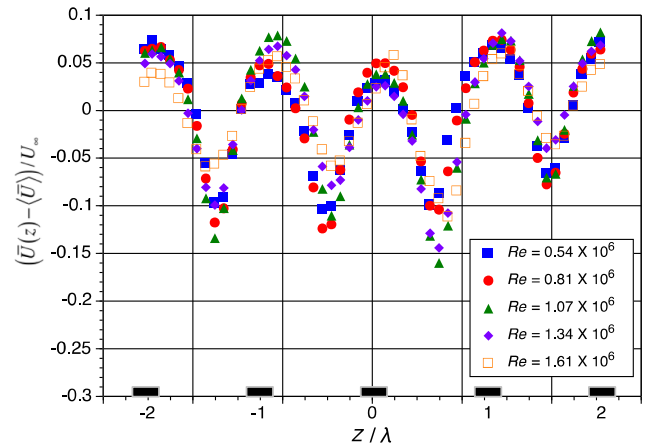


Fig. 9 Spanwise variation of scaled streamwise-component mean velocity downstream of PSVG array (40 kV case); surface electrode location indicated on abscissa.

value near the wall, u_τ^2/ν . It has been shown that the PSVG array sets up a spanwise mean velocity gradient

$$\frac{\partial \bar{U}}{\partial z} \approx O\left(\frac{\Delta \bar{U}}{\lambda}\right) \quad (5)$$

where λ is the spanwise interelectrode spacing and $\Delta \bar{U}$ is a characteristic change in the streamwise velocity component. Hence, we have the following scaling for the mean vorticity redistribution terms:

$$\bar{\omega}_y \frac{\partial \bar{U}}{\partial y} = \bar{\omega}_z \frac{\partial \bar{U}}{\partial z} \approx O\left(\frac{U_\infty}{\delta^*} \frac{\Delta \bar{U}}{\lambda}\right) \quad (6)$$

Based on measurements presented in Fig. 9, we know that

$$\partial \bar{U} / \partial z \approx U_\infty F(z) \approx O(\Delta \bar{U} / \lambda) \quad (7)$$

Hence, we have

$$\bar{\omega}_y \frac{\partial \bar{U}}{\partial y} = \bar{\omega}_z \frac{\partial \bar{U}}{\partial z} \approx O\left(\frac{U_\infty^2}{\delta^{*2}} \frac{F(z)}{\lambda}\right) \quad (8)$$

We could also obtain a similar result via an analogy to the turbulent mixing length concept. Expanding the wall-normal variation in mean velocity in a Taylor series, we have, to leading order,

$$\bar{U}(y + \ell_p) \approx \bar{U}(y) + \left. \frac{\partial \bar{U}}{\partial y} \right|_y \ell_p(z) \quad (9)$$

where $\ell_p(z)$ is a characteristic wall-normal distance that “fluid parcels” are displaced by the actuator array. Hence,

$$\Delta \bar{U} \approx \left. \frac{\partial \bar{U}}{\partial y} \right|_y \ell_p \approx O\left(\frac{U_\infty}{\delta^*} \ell_p(z)\right) \quad (10)$$

which leads to

$$\bar{\omega}_y \frac{\partial \bar{U}}{\partial y} = \bar{\omega}_z \frac{\partial \bar{U}}{\partial z} \approx O\left(\frac{U_\infty^2}{\delta^{*2}} \frac{\ell_p(z)}{\lambda}\right) \quad (11)$$

Comparison of Eqs. (8) and (11) along with Fig. 9, suggests that $F(z) \approx \ell_p(z)/\delta^* \approx O(0.1)$

Since

$$\frac{D\bar{\omega}_x}{Dt} \approx O\left(\frac{\Delta \bar{\omega}_x U_\infty}{L}\right)$$

it follows that the increase in streamwise vorticity $\Delta \bar{\omega}_x$ occurring over a PSVG actuator of length L is

$$\Delta \bar{\omega}_x \approx O\left(\frac{\ell_p(z)L}{\delta^{*2}\lambda} U_\infty\right) \quad (12)$$

This relation indicates that the mean streamwise vorticity induced by an array of active length L should scale linearly with freestream velocity due to vorticity-strain rate interaction mechanisms. Similarly, for fixed U_∞ , the streamwise vorticity increment will be proportional to the covered electrode length L .

In the following sections, the validity of this scaling is experimentally examined. To most appropriately characterize the time mean streamwise vorticity produced by the PSVG $\bar{\omega}_x \equiv (\partial \bar{W} / \partial y - \partial \bar{V} / \partial z)$, a temporal and local spatially averaged value was taken. In particular, the time mean vorticity at a particular streamwise location x , $\bar{\omega}_x(y, z)$, which is a point function, was also spatially averaged over the vortex area A_V in the local y - z plane, which was defined as the area surrounding the maximum vorticity location and bounded by the locus of points where the streamwise vorticity has fallen to 10% of

the local maximum value. Other thresholds were used and results based on the 10% threshold may be considered representative. The circulation associated with time mean streamwise vorticity

$$\Gamma \equiv \iint_{A_V} \bar{\omega}_x dA_V \quad (13)$$

is also used to characterize the actuator performance. Here A_V represents the vortex area in the y - z plane as defined earlier.

C. Effect of Freestream Velocity

Measurements were made to examine the validity of the scaling of $\bar{\omega}_x$ with U_∞ . Figure 10 presents the variation of $\bar{\omega}_x$ associated with one of the streamwise vortices produced by the PSVG as a function of U_∞ . The measurements were made at the downstream edge of the PSVG array. The experimental conditions correspond to the data set presented in Fig. 7. This figure clearly shows that $\bar{\omega}_x \propto U_\infty$ as suggested by the previous scaling argument. Also shown for reference in the figure is the mean streamwise vorticity measured at the same actuator voltage for the no-external-flow case. It is clear that mean vorticity-strain rate interaction terms serve to increase the streamwise vorticity produced by the array, as suggested in the previous scaling analysis. Figure 10 shows that that PSVGs harvest energy from the external flow and exhibit an increase in actuator effectiveness with flow speed that makes the PSVG unique among DBD plasma flow control devices. The conditions required for this behavior are discussed in the following sections.

Figure 11 presents the variation with freestream velocity of mean circulation associated with a single streamwise vortex as measured at the downstream edge of the PSVG array. These data correspond to

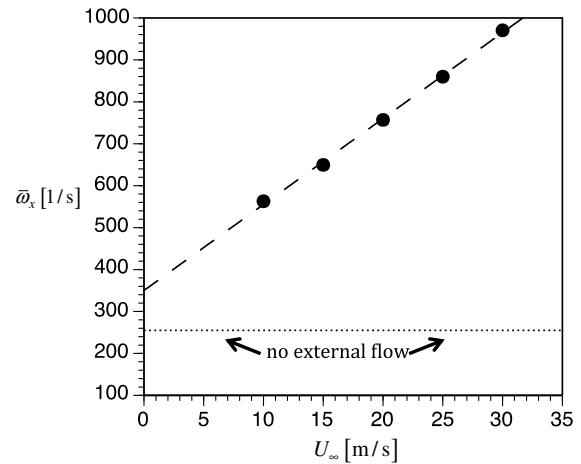


Fig. 10 Variation of mean streamwise vorticity with freestream velocity as measured at downstream edge of PSVG array (conditions correspond to those in Fig. 7).

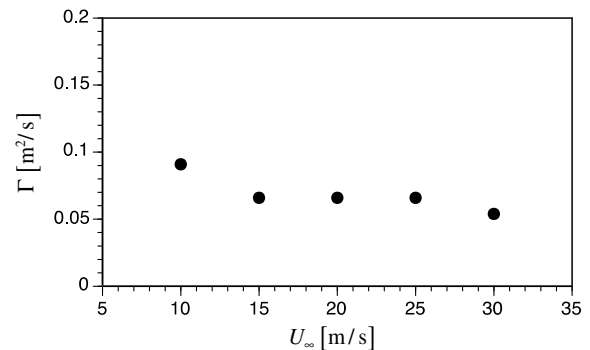


Fig. 11 Variation of mean streamwise circulation with freestream velocity as measured at downstream edge of PSVG array (conditions correspond to those in Fig. 7).

conditions identical to those for Fig. 7. Figure 11 shows that the circulation varies only weakly with U_∞ . This is fully consistent with the previous result for $\bar{\omega}_x$ shown in Fig. 10 because measurement of the associated vortex area A_V , (defined as that surrounding the local streamwise vorticity maximum and bounded by the locus of points where the streamwise vorticity has dropped to 10% of the local maximum) varies as U_∞^{-1} . For fixed covered electrode length L this indicates that the vortex area varies in proportion to the convective timescale $T_C \equiv L/U_\infty$.

D. Relevant Timescales

It has been shown that the production of streamwise vorticity by the PSVG array depends upon vorticity redistribution mechanisms, and these will require a certain minimum residence time of fluid particles over the actuator. The relevant timescales are the convective timescale $T_C \equiv L/U_\infty$ and the inverse mean strain rates S_{xy}^{-1} and S_{xz}^{-1} . The timescale S_{xy}^{-1} is set by the approach boundary layer and S_{xz}^{-1} by the PSVG array. For the actuator to be maximally effective, it must be that $T_C \geq S_{xy}^{-1}$ and $T_C \geq S_{xz}^{-1}$. For the experimental results shown in Figs. 7, 10, and 11 the convective timescale varied from $3.4 \text{ ms} \leq T_C \leq 10.2 \text{ ms}$, whereas $0.5 \text{ ms} \leq S_{xy}^{-1} \leq 0.2 \text{ ms}$ and $1.4 \text{ ms} \leq S_{xz}^{-1} \leq 3.9 \text{ ms}$. It follows that the convective timescale was always greater than the inverse strain rate timescales in the experiments. Furthermore, it is noted that $S_{xy}^{-1} \ll S_{xz}^{-1}$, which is expected to be generally true in turbulent boundary-layer flow control applications.

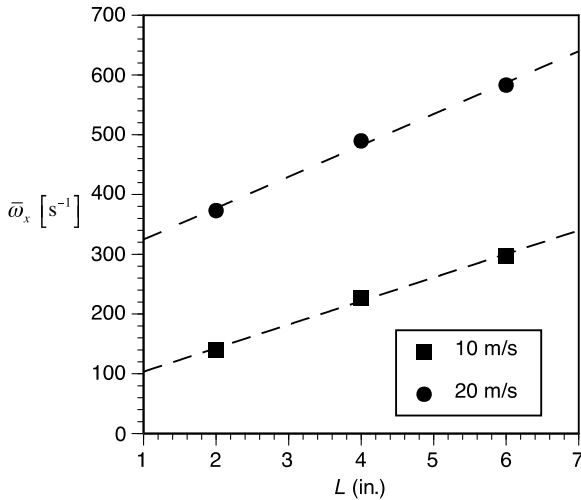


Fig. 12 Variation of $\bar{\omega}_x$ with covered electrode length L .

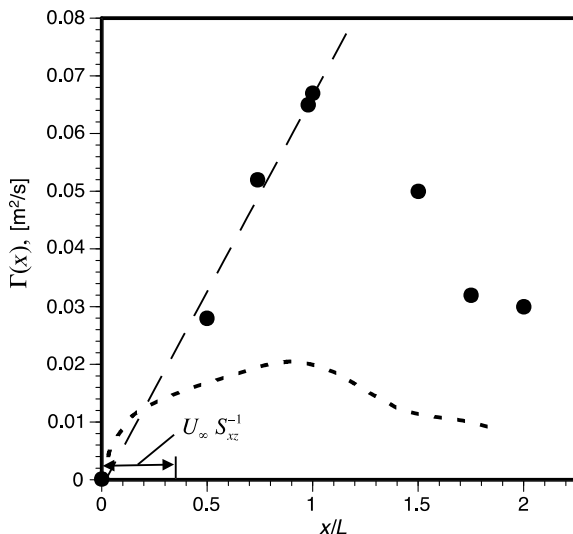


Fig. 13 Development of circulation $\Gamma(x)$ over PSVG actuator (dark circles); (dashed line) single electrode plasma vortex generator from [13].

Hence, the primary operational constraint for the PSVG becomes $T_C \geq S_{xz}^{-1}$.

E. Effect of Actuator Length

The scaling relation (12) also indicates that the augmentation of mean streamwise vorticity at fixed U_∞ is directly proportional to the length of the active electrode L . Verification of this linear variation of $\bar{\omega}_x$ with L is shown in Fig. 12, which presents the mean vorticity measured at a location 7.62 cm (3 in.) downstream of the PSVG array as a function of L for two representative values of U_∞ . To acquire these data, multiple PSVG arrays were constructed with covered surface electrode lengths of $L = 5.08, 10.16, \text{ and } 15.24 \text{ cm}$ (2, 4, and 6 in.). In each case, the spanwise interelectrode spacing was kept fixed at $\lambda = 2.54 \text{ cm}$ (1 in.), and the applied voltage was maintained at $E_{pp} = 35 \text{ kV}$. Figure 12 shows that $\bar{\omega}_x$ varies linearly with L , which is fully consistent with the scaling relation (12).

Figure 13 presents the streamwise evolution of circulation $\Gamma(x)$ associated with the production of streamwise vorticity by a PSVG array for the case of $L = 4 \text{ in.}$, $U_\infty = 20 \text{ m/s}$, and $E_{pp} = 40 \text{ kV}$. The streamwise length scale associated with the establishment of a spanwise mean velocity gradient $U_\infty S_{xz}^{-1}$ is indicated in the figure. As expected, the circulation exhibits its peak value at the downstream edge of the actuator. Furthermore, the development of circulation

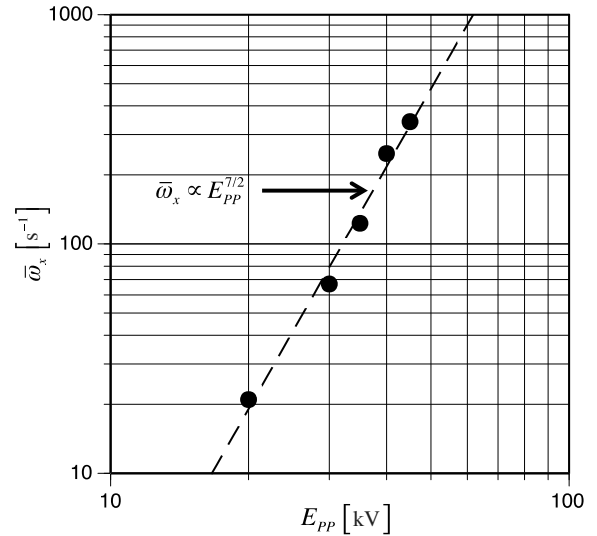


Fig. 14 Measured variation of $\bar{\omega}_x$ with actuator applied voltage for $L = \lambda = 2.53 \text{ cm}$ (1 in.), $U_\infty = 20 \text{ m/s}$.

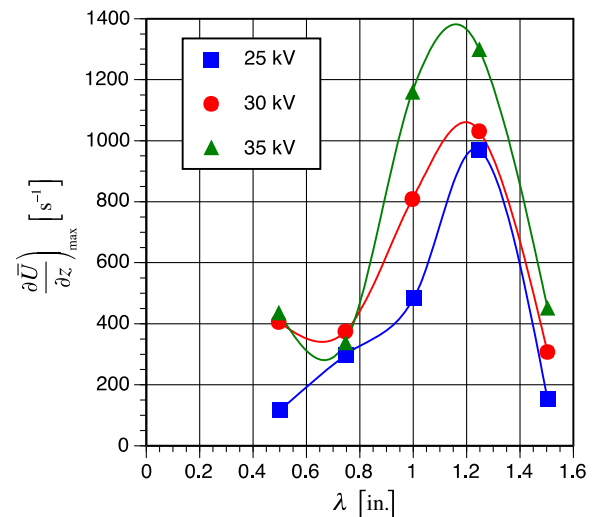


Fig. 15 Variation in $\partial \bar{U} / \partial z|_{\max}$ as a function of PSVG interelectrode spacing λ .

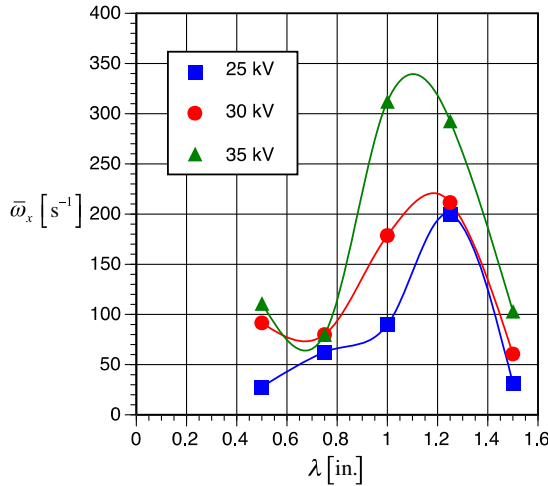


Fig. 16 Variation in $\bar{\omega}_x$ as a function of PSVG interelectrode spacing λ .

exhibits a linear variation with streamwise distance x for locations over the actuator consistent with the scaling relation (12). Downstream of the actuator, $\Gamma(x)$ diminishes due to turbulent vorticity redistribution within the boundary layer. The dashed curve in Fig. 13 shows the circulation development for the single electrode plasma vortex generator as reported in Jukes and Choi ([13] fig. 14). Aside from geometric differences in actuator geometry, the much lower peak circulation value is also consistent with the fact that spanwise vorticity redistribution mechanisms were not the primary source of streamwise vorticity production in that study. In fact, the spanwise vorticity in the approach turbulent boundary layer of the current study was 10–20 times (depending on the external flow speed) the vorticity in the laminar boundary layer of [13]. Note also that the decay of circulation downstream of the actuator is more gradual in [13] due to the laminar boundary-layer flow. In that case, turbulent vorticity redistribution mechanisms are not involved.

F. Effect of Applied Voltage

It is well known that the body force produced by DBD plasma actuators scale with applied voltage to the $7/2$ power. This scaling is embodied in current state-of-the-art actuator models (Corke et al. [4]) and has also been demonstrated experimentally (see Thomas et al. [14] fig. 5). In this section, consideration is given to how the streamwise vorticity produced by a PSVG array varies with applied actuator voltage. Figure 14 presents experimental results that document this aspect. In particular, this figure shows the variation of $\bar{\omega}_x$ with E_{pp} as measured at a location 7.62 cm (3 in.) downstream of a PSVG actuator with $L = \lambda = 2.53$ cm (1 in.). The freestream velocity was fixed at the intermediate value of $U_\infty = 20$ m/s. A least-squares power-law fit to the variation of $\bar{\omega}_x$ with E_{pp} shows clearly that $\bar{\omega}_x \propto E_{pp}^{3.5}$. Because actuator body force scales with $E_{pp}^{3.5}$, this also indicates that the streamwise vorticity produced by the PSVG array scales with the magnitude of the body force $|F_B|$. This is consistent with the vorticity redistribution mechanism described previously,

where it was shown that the streamwise vorticity increment provided by the PSVG depends proportionately upon the spanwise velocity gradient $\partial \bar{U} / \partial z$, which, in turn, is set up by the body force vector.

G. Effect of Interelectrode Spacing

Experiments were performed to assess the effect of spanwise interelectrode spacing λ on the PSVG actuator performance. For these experiments, four separate PSVG arrays were constructed for installation into the test plate, in which in the interelectrode spacing was set at values of $\lambda = 1.91, 2.54, 3.18$, and 3.81 cm (0.75, 1.0, 1.25, and 1.5 in., respectively). In each case, the covered electrode length was kept fixed at $L = 5.08$ cm (2 in.). Because it has been established that a key role of the PSVG array is to produce wall-normal vorticity through a spanwise mean velocity gradient $\partial \bar{U} / \partial z$, this quantity was measured downstream of each array, as was the mean streamwise vorticity $\bar{\omega}_x$.

Figure 15 presents values of $(\partial \bar{U} / \partial z)_{MAX}$ as measured via LDA at a streamwise location 7.62 cm (3 in.) downstream of the actuator, as a function of PSVG interelectrode spacing λ . Results for three representative applied voltages are shown. In each case, there is clearly an optimum spacing of approximately $\lambda_{OPT} \approx 3.2$ cm (1.2 in.). Note also that there is a rather abrupt reduction in $(\partial \bar{U} / \partial z)_{MAX}$ for $\lambda > \lambda_{OPT}$.

Figure 16 presents measured values of $\bar{\omega}_x$ as a function of PSVG interelectrode spacing λ . These data were acquired simultaneously with those presented in Fig. 15. Figure 16 clearly suggests that optimum performance of the PSVG in terms of mean streamwise vorticity production occurs for values of λ between 2.54 and 3.2 cm (1.0 and 1.25 in.). Again, there is a very rapid drop off in performance for $\lambda > 3.3$ cm (1.3 in.). The similarity between the variation of $(\partial \bar{U} / \partial z)_{MAX}$ and $\bar{\omega}_x$ with λ as embodied in Figs. 15 and 16, respectively, further underscores the important role played by the spanwise mean velocity gradient $\partial \bar{U} / \partial z$ created by the PSVG array in the vorticity redistribution process.

The improvement in PSVG performance with increasing interelectrode spacing for $\lambda < \lambda_{OPT}$ is associated with an increase in the (spanwise) extent of the plasma forming region on the dielectric surface and, hence, the associated body force for the range of applied voltages shown in Figs. 15 and 16. In other words, for applied voltages in the range of $25 \text{ kV} \leq E_{pp} \leq 35 \text{ kV}$ and interelectrode spacings of $\lambda = 1.27$ cm (0.5 in.) and 1.91 cm (0.75 in.), the region of surface plasma formation is artificially constrained in the spanwise extent, which, in turn, limits the body force and reduces the effectiveness of the actuator. In contrast, the loss of actuator effectiveness at interelectrode spacing $\lambda < \lambda_{OPT}$ is due to a change in the character of the colliding spanwise wall jets associated with the plasma-induced flowfield, as shown in the PIV-based vorticity fields for the no-external-flow case shown Fig. 17. In particular, for $\lambda = 1$ in., compact counter-rotating vortices are formed near the wall. In contrast, for $\lambda = 1.5$ in., the formation of coherent surface vortices is significantly reduced.

The optimum value of spanwise interelectrode spacing for both $(\partial \bar{U} / \partial z)_{MAX}$ and $\bar{\omega}_x$ is approximately equal to the local 99% boundary-layer thickness on the plate upstream of the PSVG array. That is, $\lambda_{OPT} / \delta \approx 1$. The question naturally arises whether this is

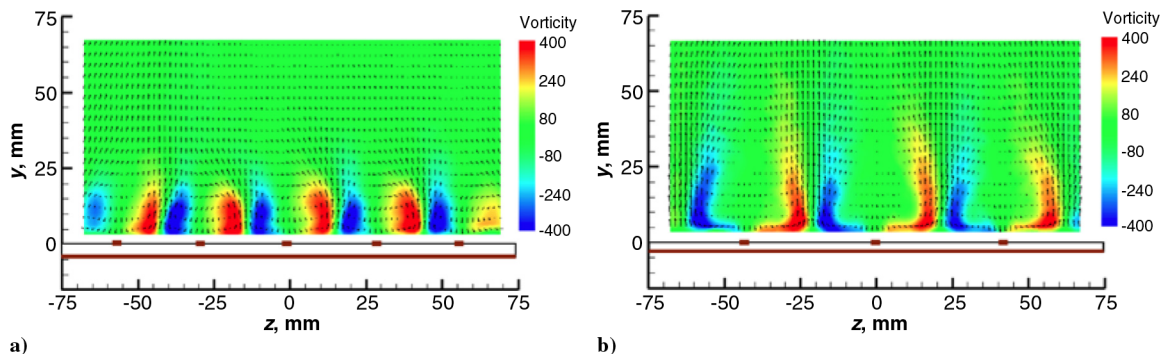


Fig. 17 Quiescent vorticity fields created by PSVG array with $E_{pp} = 40$ kV and a) $\lambda = 2.54$ cm (1 in.), and b) $\lambda = 3.81$ cm (1.5 in.).

coincidental or whether the optimum spanwise interelectrode spacing actually scales with the approach boundary-layer thickness. To investigate this, the boundary layer upstream of the PSVG array was thickened by attaching a semicircular bump (15.9 mm in diameter) near the plate leading edge, followed by a downstream section of distributed surface roughness extending 10.2 cm in the streamwise direction. This passive treatment gave rise to a separation bubble followed by turbulent reattachment, which increased the turbulent boundary-layer thickness just upstream of the PSVG array by approximately 80%. The PSVG arrays with interelectrode spacing values $\lambda = 1.905, 2.54, 3.18, \text{ and } 3.81 \text{ cm}$ (0.75, 1.0, 1.25, and 1.5 in., respectively) were again examined via LDA surveys to determine whether λ_{OPT} scaled with the new boundary-layer thickness δ . In fact, results showed no change in the optimum electrode spacing, which confirms that its value is dictated solely by the physics of the plasma discharge process (i.e., the Maxwell's equations) and is decoupled from the approach boundary-layer flow.

IV. Conclusions

Measurements presented in this paper show that the body force associated with a PSVG array generates wall-normal mean vorticity through the creation of a spanwise mean velocity gradient $\partial \bar{U} / \partial z$. This vorticity is subsequently reoriented into the streamwise direction by the imposed boundary-layer mean strain rate $\partial \bar{U} / \partial y$. In a similar manner, the spanwise mean vorticity in the boundary layer $\partial \bar{U} / \partial y$ is also reoriented into the streamwise direction by the actuator-induced spanwise mean velocity gradient $\partial \bar{U} / \partial z$. Thus, it is the product of mean strain rates $(\partial \bar{U} / \partial y)(\partial \bar{U} / \partial z)$ that is important in the production of $\bar{\omega}_x$ by the PSVG array. The interaction between the boundary layer and plasma-induced body force is shown to significantly augment the production of $\bar{\omega}_x$ over that produced by the actuator in the absence of an external flow.

The streamwise vorticity production mechanism described earlier is quite different from that outlined by Jukes and Choi [13] for their single electrode plasma vortex generator. In that case, the plasma-induced spanwise wall jet outer shear layer contained more streamwise vorticity than the spanwise vorticity in the approach laminar boundary layer. As such, vorticity redistribution mechanisms, which are key in this study, did not play as prominent a role. It is also interesting to note that the maximum mean streamwise vorticity produced by the PSVG array in the current study was $\bar{\omega}_{x,\text{MAX}} \delta / U \approx O(5000)$, whereas that reported by Jukes and Choi [13] was $\bar{\omega}_{x,\text{MAX}} \delta / U \approx O(10)$.

Scaling arguments based on the mean vorticity transport equation show, and experiments confirm, that the streamwise mean vorticity produced by the array is proportional to both the external flow speed U_∞ (for fixed L) and streamwise extent of the plasma forming region L (for fixed U_∞). For turbulent boundary layers, this scaling is expected to hold provided that $T_C \geq S_{xz}^{-1}$. Furthermore, the streamwise vorticity downstream of the actuator array is found to scale proportionately with the plasma-induced body force. Because the body force, in turn, scales with applied voltage to the $7/2$ power, there is considerable advantage to be gained by operating the PSVG arrays at high voltages. This can be accomplished by the use of thick dielectric barriers, as described in Thomas et al. [14]. The optimum spanwise interelectrode spacing does not scale with the approach boundary-layer thickness. Instead, optimum λ is governed solely by the local plasma dynamics. For fixed applied voltage, if the interelectrode spacing is too small, the spanwise extent of the plasma forming region is artificially constrained, which reduces the body force and hence the ability to produce streamwise vorticity. For too large a spacing, the local upwelling produced by colliding spanwise wall jets is negatively affected, which in turn reduces the $\partial \bar{U} / \partial z$ required for effective actuator performance.

Acknowledgments

This work was supported by Innovative Technology Applications Company, LLC under a Small Business Innovation Research Phase II Contract (N00014-11-C-0267) issued by the U.S. Department of the Navy. The authors would like to thank Judah Milgram and John Kinzer of the Office of Naval Research for their support and encouragement during this effort. The authors would also like to acknowledge Eras Noel for his important contributions to the data acquisition as well as many fruitful discussions with David Schatzman and Patrick Bowles.

References

- [1] Lin, L., "Review of Research on Low-Profile Vortex Generators to Control Boundary Layers," *Progress in Aerospace Sciences*, Vol. 38, Nos. 4–5, 2002, pp. 389–420.
doi:10.1016/S0376-0421(02)00010-6
- [2] Bushnell, D., "Longitudinal Vortex Control-Techniques and Applications," *Aeronautical Journal*, Vol. 96, No. 958, Oct. 1992, pp. 293–312.
- [3] Martin, P. B., Wilson, J. S., Berry, J. D., Wong, T.-C., Moultron, M., and McVeigh, M. A., "Passive Control of Compressible Dynamic Stall," *Applied Aerodynamics Conference*, AIAA Paper 2008-7506, Aug. 2008.
- [4] Corke, T. C., Post, M. L., and Orlov, D. M., "Single Dielectric Barrier Discharge Plasma Enhanced Aerodynamics: Physics, Modeling and Applications," *Experiments in Fluids*, Vol. 46, No. 1, 2009, pp. 1–26.
doi:10.1007/s00348-008-0582-5
- [5] Moreau, E., "Airflow Control by Non-Thermal Plasma Actuators," *Journal of Physics D: Applied Physics*, Vol. 40, No. 3, 2007, pp. 605–636.
doi:10.1088/0022-3727/40/3/S01
- [6] Huang, X., Chan, S., and Zhang, X., "Atmospheric Plasma Actuator," *IEEE Transactions on Plasma Science*, Vol. 35, No. 3, 2007, pp. 693–695.
doi:10.1109/TPS.2007.896781
- [7] Schatzman, D. M., and Thomas, F. O., "Turbulent Boundary Layer Separation Control Using Plasma Actuators," *AIAA Journal*, Vol. 48, No. 8, 2010, pp. 1620–1634.
doi:10.2514/1.J050009
- [8] Kozlov, A. V., and Thomas, F. O., "Flow Control via Two Types of Dielectric Barrier Discharge Plasma Actuation," *AIAA Journal*, Vol. 49, No. 9, 2011, pp. 1919–1931.
doi:10.2514/1.J050793
- [9] Kozlov, A. V., and Thomas, F. O., "Plasma Flow Control of Cylinders in a Tandem Configuration," *AIAA Journal*, Vol. 49, No. 10, 2011, pp. 2183–2193.
doi:10.2514/1.J050976
- [10] Okita, Y., Jukes, T., Choi, K.-S., and Nakamura, K., "Flow Reattachment over an Airfoil Using Surface Plasma Actuator," *AIAA Paper* 2008-4203, 2008.
- [11] Jukes, T. N., Segawa, T., and Furutani, H., "Flow Control on a NACA 4412 Using Dielectric-Barrier-Discharge Vortex Generators," *AIAA Journal*, Vol. 51, No. 2, 2013, pp. 452–464.
doi:10.2514/1.J051852
- [12] Jukes, T. N., and Choi, K.-S., "Dielectric Barrier-Discharge Vortex Generators: Characterization and Optimization for Flow Separation Control," *Experiments in Fluids*, Vol. 52, No. 2, 2012, pp. 329–345.
doi:10.1007/s00348-011-1213-0
- [13] Jukes, T. N., and Choi, K.-S., "On the Formation of Streamwise Vortices by Plasma Vortex Generators," *Journal of Fluid Mechanics*, Vol. 733, Oct. 2013, pp. 370–393.
doi:10.1017/jfm.2013.418
- [14] Thomas, F. O., Corke, T. C., Iqbal, M., Kozlov, A., and Schatzman, D., "Optimization of SDBD Plasma Actuators for Active Aerodynamic Flow Control," *AIAA Journal*, Vol. 47, No. 9, 2009, pp. 2169–2178.
doi:10.2514/1.41588
- [15] Klebanoff, P. S., "Characteristics of Turbulence in a Boundary Layer with Zero Pressure Gradient," *NACA TR-1247*, 1955.

A. Naguib
Associate Editor